Micromechanical investigation of grouting in soils

Boschi, Katia; Di Prisco, Claudio; Ciantia, Matteo Oryem

Published in:
International Journal of Solids and Structures

DOI:
10.1016/j.ijsolstr.2019.06.013

Publication date:
2019

Micromechanical investigation of grouting in soils

Katia Boschi , Claudio Giulio di Prisco , Matteo Oryem Ciantia

PII: S0020-7683(19)30290-2
DOI: https://doi.org/10.1016/j.ijsolstr.2019.06.013
Reference: SAS 10403

To appear in: *International Journal of Solids and Structures*

Received date: 4 June 2018
Revised date: 26 April 2019
Accepted date: 14 June 2019

Please cite this article as: Katia Boschi , Claudio Giulio di Prisco , Matteo Oryem Ciantia , Micromechanical investigation of grouting in soils, *International Journal of Solids and Structures* (2019), doi: https://doi.org/10.1016/j.ijsolstr.2019.06.013

Micromechanical investigation of grouting in soils

- Author 1/Corresponding author

  Katia Boschi, Politecnico di Milano (Milan, Italy)
- Author 2

  Claudio Giulio di Prisco, Politecnico di Milano (Milan, Italy)
- Author 3

  Matteo Oryem Ciantia, University of Dundee (Dundee, United Kingdom)

Abstract

Grouting and jet grouting are geotechnical consolidation techniques commonly employed to improve the mechanical behaviour of soils. Although these techniques are common, the micromechanical processes taking place at the local level are not yet totally understood and modelled. In this work, such a problem has been approached from a micromechanical perspective via the discrete element method by considering the local interaction among soil grains and pseudo-fluid particles. Homogeneous representative elementary volumes of a virtual analogue of silica sand have been first generated and tiny rigid frictionless particles have been subsequently injected through them, to simulate the grouting in granular materials. Various injection pressures, initial soil pressures and initial soil densities have been considered. The different diffusion patterns, the flow rate, the consequent increase in local stresses and the consequent reduction in local porosity have been discussed. To overcome the DEM computational restrictions and to speed up the injection simulations, a novel procedure based on the replication of pre-equilibrated cells has been adapted for both the initialization and injection phase. Finally, a qualitative laboratory-scale pressure grouting test has been reproduced to validate the results.

Key Words: Soil Mechanics, Micromechanics, Numerical Analysis, DEM, Grouting.

1. Introduction

Pressure grouting is a stabilization technique for improving ground mechanical properties implying the injection of a fluid-like material under controlled pressure at strategic locations into soil strata via single or multiple ports. Grout pressurization into the soil can be performed through holes or pipes drilled, jetted or driven at the desired location and so may take the form of permeation grouting, jet grouting, compaction grouting or fracture grouting (Dayakar, 2012; Wang et al., 2009, 2013, 2016). Regarding jet grouting design applications, the fundamental factors to be taken into account are grout mix, jet nozzle energy, grout flow rate, grout rod rotation and withdrawal rates (Munfakh et al., 1987; Covil and Skinner, 1994).

From a geotechnical engineering perspective, the design is predominantly derived from empirical approaches based on experimental observations, including ground heave during injection; the effectiveness is sometimes verified by field pull-out tests (Yin et al., 2005). Due to the complexity of the coupled hydro-mechanical processes governing the injection, the final characteristics of the grout bulb are generally unknown. Moreover, phenomena like shortfall in consolidation, consolidation occurring at unexpected locations or high pressure induced ground cracking can occur (Paans, 2002).

To improve and tune design parameters, in jet grouting applications in situ tests are performed: the visual observation of the grouted volume after excavation allows to determine the equivalent column diameter and, owing to lab tests, characterise mechanically the grouted soil. The geometry of the columns can also be detected by means of (i) DC electrical resistivity push probes (Frappin and Morey, 2001; Madhyannapu et al., 2009; Bearce et al., 2015) and (ii) temperature measurements (Meinhard et al., 2010). By associating temporal and spatial changes in density with changes in the mechanical response, the soil density detection approach can be employed (Morey, 1992) to assess the mechanical properties of the grouted material. All these techniques are time consuming and their costs make very often jet grouting not competitive if compared with alternative geotechnical solutions.

Owing to the technological improvements of the last decades, in the lab the internal structure of soils can be visualized by means of X-ray tomography (Desrues et al., 2010). This technique was employed for grout injection problems by Bezuijen and Van Tol (2006). Wang et al. (2016; 2017) performed laboratory-scale pressure grouting tests on loose sands under confined boundary conditions, varying the grout water/cement ratio, the injection pressure and the soil degree of saturation. They also investigated changes in the grout bulb characteristics and grout diffusion patterns by means of photo-based 3D photogrammetry. Nishimura et al. (2011) experimentally examined the variation in stresses by simulating compaction grouting processes in a geotechnical centrifuge. An assembly of soil container and grout injection system was so mounted on the centrifuge platform and subjected to centrifugal acceleration. A suitable mixture of Soma silica sand, Kawasaki clay, Portland cement and water at different ratios was then injected in Soma silica sand. They took into consideration various initial soil relative densities, hydraulic conditions and pile spacing.

Over recent years, to obtain more accurate predictions, few models and design methodologies have been proposed and a review about jet grouting was provided by Ribeiro and Cardoso (2017). Theoretical models have been suggested by Modoni et al. (2006) and by Wang et al. (2012). These are derived from the free turbulent submerged jets theory. The approach followed by Flora et al. (2013) can be considered to be semi-theoretical. The ratio between the average diameter of the jet column and the one of a reference scenario, for which all the parameters considered in the model are well known, is assumed to be proportional to the erosive capacity of the jet and inversely proportional to the soil resistance to erosion.

The use of advanced continuum framed numerical methods to study fluid-soil interaction problems is becoming more popular. Modoni et al. (2015) used the finite volume method to model a jet injection under turbulent flow regime on fluid having the composition of a fresh jet column (mixture of injected fluid(s), ground water and soil particles). Starting from Bui and Sako (2007), who analyzed soil–fluid interactions by means of a water jet, several studies (Stefanova et al., 2012; Bozhana Stefanova et al., 2012; Guo et al., 2013) confirmed that in future the smoothed particle hydrodynamics (SPH) method may be used to simulate the jet grouting injection. The SPH method, due to its particle-based nature, has also been used to model hydraulic erosion and sediment flushing (Krištof et al., 2009; Manenti et al.,

2011) and therefore may be extended to assess the erosive action of fluid jets into the ground.

Within a micromechanical particulate framework, a coupled computational fluid dynamics (CFD) and DEM modelling approach could also be used to better capture sand-grout interactions during injection problems. However, due to the large number of particles and the high injection speed, a DEM-CFD coupling would lead to very high Reynolds numbers and hence very challenging numerical issues and unacceptable computational costs (Chen and Wang, 2014). The limitation in terms of computational costs also discourages the use of Lattice-Boltzmann (LB) and DEM coupling (Leonardi et al., 2014). Pore scale finite volumes (PFV) and DEM (Chareyre et al., 2012; Catalano et al., 2014) coupling would allow both to capture local effects and to handle reasonable computational times but only for quasi-static analyses and, therefore, would be more appropriate to model low pressure permeation grouting. A big challenge for all the above-mentioned methods is the presence of micro-grains composing the grout which strongly affect the rheology and the overall flow within the porous soil.

In this paper, the grout injection problem is hence addressed numerically by means of a novel micromechanical approach overcoming some of the previously mentioned limitations that may be faced with CFD-DEM, LB-DEM, PFV-DEM coupled models. In order to remain in a non-coupled framework, a simplified method to account for local interactions among soil grains and high-pressure injected grout is proposed. Whilst DEM is well suited to simulate granular media and their behaviour under static, transient and dynamic conditions, the main simplifying assumption hereafter introduced is to model the injected grout as an assembly of rigid tiny frictionless particles. In line with what observed numerically in the last 20 years by many authors belonging to the fluid mechanics community (Peyneau and Roux, 2008; Hatano, 2008; Otsuki and Hayakawa, 2009; Chialvo et al., 2012; Vescovi and Luding, 2016) the rheology of this frictionless granular material is found to be in fair agreement with real grout mixtures (Boschi, 2018), at least for sufficient small values of particle velocities. The numerical results obtained by the authors and presented here in the following confirm this last hypothesis.

In the following, after generating and testing a virtual sand DEM model (PS), the approach used to represent the grout is illustrated. Finally, laboratory scale experimental tests

concerning the pseudo-fluid (PF) or mixtures of PF and PS are numerically reproduced. All the simulations discussed in this paper are performed by using the PFC3D software (Itasca, 2017).

2. DEM model of sand REVs

Homogeneous cubic representative elementary volumes of untreated ideal loose and dense silica sand (PS) are generated inside six frictionless rigid walls, by adopting the radius expansion method. The choice of using frictionless walls to study the volumetric response of a DEM sample is driven by the fact that the same DEM sample will be employed in the following to simulate injection tests. By means of a servo-controlled mechanism, a 5 kPa isotropic stress is imposed and, by adjusting friction coefficient, the target porosities (n) are obtained: n = 0.42 corresponding to loose and n = 0.39 to dense PS specimens. PS mimics a Fontainebleau silica sand characterized by a grain density (ρ_s) of 2.65 g/cm^3, D_{50} of 0.21 mm and a coefficient of homogeneity ($Cu=D_{60}/D_{10}$) of 1.57. To fill a 111 mm^3 specimen 19662 particles are used in the dense case, while in the loose one 19580 particles are contained in a 141 mm^3 box. Particle-particle and particle-wall interactions are modelled by using the Hertzian contact law. The adopted microscopic parameters, taken from Ciantia et al. (2016b), are reported in Table 1. To get the steady-state regime in a reasonable number of cycles, all the simulations on PS REVs employ a local non-viscous damping coefficient α^* of 0.05 (Cundall, 1987). This "body-based" damping scheme is available in PFC3D to artificially remove additional kinetic energy (Itasca, 2017) and often adopted in quasi-static simulations. In this case, the solution obtained is independent of the α^* value (Ciantia et al., 2016b).

Once the specimens are equilibrated at the target stress and porosity, to capture the macroscopic behaviour of a real material, the simplifying assumptions of fixing particle rotation and tuning the contact friction coefficient are adopted (Ting et al., 1989; Calvetti, 2008; Arroyo et al., 2011; Ciantia et al., 2018). The recent micro-CT measurements by Rorato et al. (2017) suggest that particle rotation is not very important before strain localization. In agreement with what already done by many other authors, to show the capability of the model of capturing the experimental mechanical behaviour of both dense and loose sands, in Figure 1 the responses of numerical specimens loaded under drained standard triaxial compression tests are reported.

3. Modelling a pseudo-fluid phase via DEM

This work proposes to model the cement grout via DEM by employing very small rigid frictionless particles. To allow infiltration of PF throughout the voids of the PS specimen in paragraph 4, the D_{100} of PF is set to be equal to $0.18D_0$ of PS (Kenney et al., 1985). The particle size distribution (PSD) for PF employed by the authors is so characterized by a D_{100} of 0. 0225 mm. In Figure 2 this is compared with the PSD of PS. The authors employ a grain density, ρ_s, equal to 3.7 g/cm3 to obtain a macroscopic density comparable with the density of cement grouts characterized by low w/c ratios (0.5), i.e. ranging from 1.8 to 2.3 g/cm3 (BASF, 2015). Any contact formed among PF particles is governed by a linear law (Table 2). To simulate the mechanical behaviour of a fluid-like material, both friction coefficient, μ, and damping along the tangential direction, β_s, are set to zero, whereas the value of damping along the normal direction, β_n, is imposed equal to 0.2. Also for PF particles the rotation is inhibited. Nevertheless, the effect of fixing rotations of the PF particles is found not to affect the numerical results of the injection tests (Boschi, 2018). Furthermore, the contact law chosen to rule the PS-PF interaction is a Hertzian one and the correspondent parameters are in Table 3.

The capability of the DEM PF model to reproduce the main features of a particulate viscous fluid such as cement grout is first addressed by testing the frictionless granular material at the volume level. A PF REV, composed by 22327 particles, is generated by following the same approach previously described. An internal porosity of 0.37 is imposed. This value is calculated by considering an internal measurement sphere and, so, disregarding boundary effects. Wall-ball contacts have the same properties of the ball-ball ones (Table 2).

Consolidated drained triaxial compression tests are performed on this specimen and the results are compared with PS behaviour (Figure 3) in terms of stress ratio, $\eta=q/p'$, and volumetric strain, ε_{vol}. The shear strength at critical state for PF is 15% of the PS one. This corresponds to a macroscopic friction angle of 5°. The changes in volumetric strain are negligible with respect to the values experienced by PS under loose and dense conditions.
Despite the particle-particle coefficient of friction is nil, interlocking and jamming effects are responsible of the macroscopic frictional strength observed. They are induced by the choice

of employing particles to simulate the fluid phase and the high density, at which PF specimens are generated to model a quite incompressible fluid, respectively. Since the initial shear strength of viscous mortars is different from 0 and increases quickly as a consequence of physical interactions of various constituents and mutual chemical reactions (Raivio, 2007), PF employed by the authors seems to simulate suitably the rheology of grout.

To further test the capability of PF DEM model to capture the main traits of a viscous fluid phase, the following laboratory scale experimental test is simulated. A 2 x 2 x 5 mm^3 vertical column of PF particles is equilibrated under the effect of gravity, its side wall is then deleted and the system is let to flow in a 4 mm wide box. The temporal evolution of the particulate system is in accordance with the expected fluid behaviour (Figure 4) and the final spatial distribution of particles and contact forces is shown in Figure 5. As is reported in Figure 6, a fairly uniform porosity of 0.37 is detected in the middle of the specimen and the well-known effect of rigid walls on porosity is also clearly visible. The initial and final distributions of pressure acting on the side walls are fully in agreement with the analytical ones (Figure 7). Once again, the interlocking effect induced by the particulate nature of PF is responsible of the 5° angle of natural repose (Figure 5), coinciding with the critical state friction angle derived from the TX-CD test.

4. DEM modelling of pseudo-fluid injection in granular material

In this section the above described PF is going to be injected into the cubic specimens filled with PS, whose mechanical response has been discussed in paragraph 2. These specimens are created by imposing an initial pressure on all the six faces. During the injection phase, the walls are fixed. PF diffusion, changes in both stress and porosity within the specimen and flow rates are put in relation with (i) injection pressure, p_{inj}, (ii) initial PS porosity, n_{sand}, and (iii) initial PS isotropic pressure, p_{sand}. All results are obtained by assuming: (i) PF does not cure during the injection and hence cementation effects are disregarded, (ii) gravity is set to zero.

To simulate the injection process, a PF square cross-section rigid frictionless tube is generated by employing the cell repetition method (Ciantia et al., 2017; 2018). A servo-controlled wall (wall A in Figure 8) is employed to impose its initial pressure equal to the

injection one, p_{inj}. The test starts when the wall separating PS and PF (wall B) is erased. While PF penetrates into PS, the servo-mechanism keeps the stress on wall A to be constant. Table 4 summarises the set of numerical tests performed, corresponding to loose and dense specimens, various injection pressures and various initial PS pressure. The timestep employed is automatically imposed by PFC3D software (Itasca, 2017).

4.1 Numerical results

In all the tests discussed in this section, the injected volume is equal to 0.48 mm^3 of PF. The test stops the instant of time immediately after the injection of the target PF quantity. In Figures 9, 10 and 11, initial and final layouts for PS and PF, in case of dense and loose specimens corresponding to p_{inj} of 600 kPa and p_{sand} of 5 kPa, are compared. In particular in Figure 9 the PF spatial distribution along x and z direction is illustrated in a central portion of thickness equal to the tube thickness. In Figure 10 PS particle induced displacements in the same portion are reported, whereas in Figure 11 the contact force networks in the whole specimen are illustrated. A qualitative analysis of all the injection simulations reveals the formation of two different diffusion processes developing within PS:

- mechanism PFB associated with dislocation of PS grains leading to the formation of a PF bulb;
- mechanism PFP in which the PF particles penetrate within the pores without severely changing the initial microstructure of PS.

As is evident from Figure 9, when the initial density is sufficiently large (Figure 9a), mechanism PFP prevails with respect to the first one. The dimensions of the bulb are very small and most of PF is infiltrating into the pores of the medium. Preferential paths along the wall boundaries, where the porosity is higher, are evident. In contrast, in case of loose specimens, mechanism PFB prevails and a well pronounced bulb develops. Such an observation is confirmed by Figure 10: the amplitude of the displacement vector of each grain is quite larger in case of Figure 10b (loose condition) with respect to Figure 10a (dense condition). In fact in the loose specimen the wider void space is such that PS particle rearrangement is less constrained, while in the other specimen the dense fabric itself inhibits PS particle displacements. Such constraint results into a higher increase in contact forces induced by PF injections with respect to the loose case (Figure 11). Finally, it is worth noticing that the process of injection induces a large increase in contact forces in the

"nearfield" but also in the entire specimen due to the fact that the walls on the boundaries are imposed to be still and rigid.

From a quantitative point of view, the effect of initial PS density and injection pressure on PF diffusion patterns is shown in Figure 12 for the 5 kPa p_{sand} case. By assuming axisymmetric conditions with respect to the injection direction, the ratio between the volume of PF in each cylindrical crown and the corresponding total cylindrical crown volume is reported. The observations referred to Figure 9 are confirmed. Moreover, varying the injection pressure from 300 kPa to 600 kPa at constant PS density, the PF penetration increases in the injection direction as it is clearly visible in the dense case. In the loose one the increase in penetration is limited due to the proximity of the rigid wall to the PF front.

After the injection, pore spatial distribution has evolved and a part of pores has been filled by PF particles. Since the boundaries of the cube are kept fixed during injection, the evolution of spatial distribution of PS grains is experienced by the material as a loss in homogeneity but not as a change in the mean value of its volume. In contrast, since PF particles are here interpreted as a grouting mixture, after the injection a new internal porosity variable (n*) has to be defined. This takes into account both PS and PF particles. In Figure 13 the local variations in porosity, $\Delta n^* = n^*_{fin} - n_{ini}$, in the loose and dense cases are compared for p_{inj} = 300 kPa and p_{sand} = 5 kPa. In particular, contours of Δn^* related to a slice of the specimen perpendicular to the injection direction (Figure 13a) and a central slice parallel to the injection direction (Figure 13b) are illustrated. The thickness of the two slices is $1/3^{rd}$ and $1/5^{th}$ of the box size, respectively. The whole area of major influence in the former case is analysed. In the latter one only the zone close to the injection tube along the transversal direction is considered. In both cases a reasonable representative number of particles is contained by each averaging volume (O'Sullivan, 2014). In accordance with what already observed in terms of PS particle rearrangement and PF spatial distribution, the dense specimen shows a higher but concentrated densification in correspondence of the injection region, while the compaction under loose condition is more distributed along all directions.

Contours of change in isotropic pressure, considering only PS particles, normalised with respect to p_{inj} are reported in Figure 14a and Figure 14b (case of p_{sand} equal to 5 kPa) for the previous slices perpendicular and parallel to the injection direction, respectively. In the porosity contours, the solid volume calculation properly accounts for particles crossing the averaging cube boundaries. On the contrary, for the average stress state within each portion, the particle representative stresses are weighted for their own total volume only when their centre belongs to the averaging volume in exam. While the variations in stresses concentrate mainly around the injected bulb under loose condition, for the dense case the increase in stress state is systematically larger and affects significantly the whole specimen. By increasing p_{inj} at constant PS density, the increments in stress in PS are larger. The effect is more evident under dense conditions.

In Figure 15, relative to initial PS pressure of 100 kPa and p_{inj} of 600 kPa, the spatial distribution of PF particles (Figure 15a) and contours of change in PS isotropic pressure normalised with respect to p_{inj} (Figure 15b) are reported. By increasing considerably p_{sand} (from 5 kPa to 100 kPa), the dislocations of PS grains are inhibited and it is observed that mechanism PFP tends to prevail. As PS stress state evolution is concerned, at long distances the increase in pressure is higher with respect to 5 kPa p_{sand} case, at the injection proximity the opposite reasonably occurs. These effects can be observed by comparing the sub-figures of Figures 12, 14 and 15 characterized by the same p_{inj}, n_{sand} but p_{sand} equal to 5 kPa in Figures 12 and 14 or 100 kPa in Figure 15.

In practical applications, in order to determine the injectable grout volume, it is important to provide information and predictions about flow rate evolutions. In Figure 16a, the dependence on PS density, p_{sand} and p_{inj} of the mean flow rate for injecting 0.48 mm^3 of PF is shown. Actually, in these plots, instead of flow rate Q, its normalization, q, with respect to the cross-section area of the fluid tube is considered. Reasonably, by increasing PS density and initial pressure and by decreasing injection pressure, the dislocation of PS grains is inhibited and the average q, q_{mean}, reduces. For significantly high injection pressures (6000 kPa) the dependence of q_{mean} on initial PS stress state and density becomes less evident. By interpolating the points, associated with constant values of p_{sand} and PS density, different lines are obtained. These are characterized by different curvatures and they depend on the

type of mechanism governing the process. For the sake of clarity, the evolutions of flow rate normalized with respect to the corresponding q_{mean} values, during all the simulations mentioned in Figure 16a, are reported in Figure 16b. Different trends are also obtained depending on the predominant diffusion pattern. In case of dense conditions with p_{sand} of 5 kPa and p_{inj} of 300 kPa or with p_{sand} of 100 kPa and p_{inj} of 600 kPa, the initial peak in q is due to a size effect. In fact, the tube width is comparable with grain dimensions. Under in situ conditions, the peak is expected to disappear, since the ratio of tube width over grain dimensions severely increases. Penetration of PF within PS voids (mechanism PFP) governs the process and q reduces more and more while increasing the ideal radius of the PF front. In case of dense PS with p_{sand} of 5 kPa and p_{inj} of 600 kPa or in case of loose PS with p_{sand} of 100 kPa and p_{inj} of 600 kPa, after the initial peak due to the previously mentioned size effect, an oscillating trend testifies the attempt of both mechanisms to prevail one on each other. At the end mechanism PFP seems to prevail. In the other cases, q increases faster and faster, PS grains dislocate and the bulb dimensions grow.

4.2 *Enhancing computational efficiency of injection*

The computational time required to complete each injection simulation is of several hours. Considering for example the dense box at 5 kPa with p_{inj} of 600 kPa, the computational time, required to inject 0.48 mm^3 of PF, is of 32 hours. By disregarding the CPU processing speed and the timestep chosen which for these analyses are fixed, the factors influencing the computational time are both the injection pressure and the total number of particles. Since the injection pressure is a fixed boundary condition, the only way to speed up the simulation is to decrease the number of particles. To achieve this, the cell repetition method (CRM), proposed by Ciantia et al. (2017; 2018) for large-scale model generation, is adapted also for the injection phase. The total number of particles in the model is reduced by injecting smaller PF volumes one after the other (Figure 17). By the end of the simulation, the same total volume of PF (V_{inj}) will be injected but, since the total number of particles in the model gradually increases, the computational time will reduce. To employ the CRM, so, a smaller PF specimen is first generated and equilibrated at the desired p_{inj} pressure. The corresponding particle location and contact forces are then saved. During the injection, once the constant pressure servo-controlled wall reaches the PS box boundary, i.e. PF has all

been injected, the initial PF specimen is re-generated and the previous wall moved to the original position for another injection phase.

In Figure 18a the computational time of three injection simulations are compared. One considers the injection of a 3 mm long fluid tube without adopting CRM, while the other two employ CRM by replicating a 0.7 mm and 1.5 mm long fluid tube, respectively. Whilst in the first case the number of particles is constant, in the two PF-CRM models the number of particles increases gradually (Figure 18b). As is evident, CRM reduces the model computational time but when PF is replicated, the PS specimen experiences a slight drop in pressure. The fact of translating instantaneously servo-controlled wall A, from the sand sample proximity to a higher distance during the time step of the CRM application, causes a short-lived decrease in both the just injected PF contact forces and the PS ones closed to the injection tube. The pressure drops reflect macroscopically this effect. These pressure drop trends are reported in Figure 19. On the other hand, by reducing the length of the fluid tube these pressure drops can be limited and higher pressures can be imposed to the specimen also for low injection volumes. The 0.7 mm PF-CRM has more frequent pressure drops characterized by a lower amplitude with respect to the 1.5 mm model. As V_{inj} increases, the pressure tends to the same value independently of the approach used.

5. Application of the pseudo-fluid model to laboratory-scale injection experiments

To analyse the grout evolution and diffusion process upon pressure grouting injection in a silica sand from Stockton Beach (Australia), Wang et al. (2016) carried out laboratory-scale tests on a loose sand (n equal to 0.45) under confined boundary conditions adopting different grout water/cement ratios (0.5 and 1) and soil degrees of saturation (ranging from 5% to 60%). To numerically simulate these tests by using a DEM model (Figure 20), a specimen with 29975 particles is prepared: a "cloud" of close but not-in-contact particles using the random number generation approach is generated in a cylindrical chamber (100 mm radius and 300 mm height). Subsequently, gravity (9.81 m/s^2) is applied and particles settle. More precisely, with the aim of guaranteeing an acceptable specimen homogeneity, the specimen is subdivided in 100 mm thick strata and each stratum is generated after the other. Following Arroyo et al. (2011) and similarly to Ciantia et al. (2014, 2016a), the material PSDs have been magnified to reduce the final number of particles filling the

chamber. The factor of magnification imposed is 38. The contact parameters are the same of the one employed to obtain the results in previous sections but, to create the loosest possible specimen, a higher friction coefficient (0.4) is initially imposed during the specimen preparation. Once a quasi-static condition is reached, the friction coefficient is reduced to 0.38 and a new quasi-static condition is got. The procedure is repeated step by step until the desired friction coefficient value of 0.275 is attained. In order to allow the insertion of the injection pile within the chamber a hole with a 16 mm diameter and 160 mm height is generated by deleting a certain number of particles. The cylindrical injection tube (10 mm in diameter and 150 mm in internal length) is then inserted and the new static conditions are obtained. An average internal porosity of 0.43 is obtained by disregarding boundary effects. After checking the homogeneity in terms of both particle spatial distribution and contact forces, the PF injection phase starts by following the same method described in section 4.2. The simulation is performed by imposing a p_{inj} of both 100 kPa and 300 kPa (Figure 21). In the former case, the volume of PF injected is equal to 143 cm^3, in the latter one equal to 159 cm^3.

The induced displacements in PS particles are considerably larger with respect to the previous numerical simulations in the PS box (2 orders of magnitude larger). This may be justified by considering that in this case (i) the initial applied stress is lower, (ii) the initial porosity is larger and (iii) no volumetric constrain is imposed to the volume of the box.

To qualitatively compare the numerical results with the experimental ones, two volumes are taken into consideration. A volume is 15 mm thick and the two remaining dimensions coinciding with the horizontal dimensions of the model. It is located at a depth corresponding to the maximum radial dimension of the bulb. The second volume considered is 15 mm thick and characterised by height and width coinciding with the model ones. This volume is located symmetric with respect to a vertical radial plane. In Figure 22 a view corresponding to the previously defined volumes for the two different injection pressures after the injection of 143 cm^3 of PF is shown. It is evident an enlargement of the injected bulb at increasing injection pressures. For the injection at 300 kPa the bulb penetration is deeper along the z direction. In case of 100 kPa a higher quantity of PF particles can infiltrate deeply through PS voids due to a smaller induced compaction of PS particles in the injection proximity. Analogously, Wang et al. observed that the injected grout volume

increases about linearly with the grouting pressure and that an increase in the grouting pressure leads to an enlarged grout bulb dimension for both w/c ratios.

Again in agreement with lab results, a general density increment is obtained. Porosity contours before and after injection in the two DEM simulations are reported in Figure 23. Axisymmetric conditions with respect to the injection direction are assumed and 2D contours are obtained as a function of z (distance from the bottom wall) and ρ (distance from the pipe axis) coordinates. Rigid walls cause an unavoidable increase in porosity in their proximity. The increase in porosity that can be detected, instead, in proximity of ρ=0mm for z>140mm is due to the presence of the pipe, which is empty before and after injection. For p_{inj} = 300 kPa and V_{inj} = 159 cm^3, the reduction in porosity is higher but mainly concentrated in the bulb proximity.

6. Conclusions

From a mechanical viewpoint, the injection of grout in a granular material is a complex process that from a numerical modelling perspective finds various challenges including large displacements and deformations, localized flows and particle fluid interaction to name a few. In this paper the grout injection is simulated via the discrete element method. In particular, the grout is here modelled by employing sufficiently small rigid frictionless particles. From the results of the numerical simulations it is found that:

- a pseudo-grout specimen subject to consolidated drained triaxial compression tests behaves like a quite incompressible material characterised by a low shear strength;
- when simulating the discharge of a pseudo-grout column within a closed box using this approach, the results are in agreement with analytical and experimental expectations in terms of both pressure and porosity distributions. The angle of natural repose coincides with the critical state friction angle.

Considering injection problems of pseudo-grout in cubic specimens filled with a virtual analogue granular material, the authors observe that:

- under dense conditions the infiltration phenomenon throughout soil voids prevails, while under loose conditions the dislocation of solid grains prevails and a pseudo-grout bulb grows;
- the loose specimen is characterized by larger induced displacements of solid particles and the dense one by the higher increase in the stress state;

- an increase in injection pressure causes an obvious increase in terms of pseudo-grout penetration, solid grain dislocations and stresses. These effects are more evident in the dense case;
- by increasing the initial soil pressure, a penetration diffusion pattern tends to prevail, the increase in the solid grain stress state is lower at the injection proximity, the opposite occurs at long distances;
- the time required to inject a fixed pseudo-grout volume reduces by increasing soil density and initial pressure and by decreasing injection pressure. A different flow rate trend is reached depending on the predominant diffusion pattern: when penetration of pseudo-grout within pores prevails, the flow rate reduces. When dislocation of solid grains and formation of a pseudo-grout bulb prevails, the flow rate tends to increase more and more rapidly.
- the adoption of the cell repetition method for both the initialization and injection phase can considerably speed up the computational time.

A further confirmation of what stated here above has derived from a comparison between numerical results obtained by the authors and experimental data already published in literature.

Research on this line offers room for many improvements and, in particular, the inclusion of grout cohesion and the transient nature of the rheological properties of the injected grout. Within a DEM framework this could be achieved by activating particle bonds between PF-PF particles and between PF-PS particles. A temporal dependence of bond activation and of bond strength and stiffness should be implemented.

7. Tables

Table 1. Hertz model microscopic parameters referred to PS particles with μ the friction coefficient, ν the Poisson's ratio and G the shear modulus. The subscript 'b' stands for ball-ball contacts and 'w' for wall-ball contacts.

μ_w [–]	μ_b [–]	ν_w [–]	ν_b [–]	G_w [kPa]	G_b [kPa]
0.0	0.275	0.3	0.3	3e6	3e6

Table 2. Linear model microscopic parameters referred to PF particles with E* the effective modulus, k* the normal-to-shear stiffness ratio, μ the friction coefficient, β_n and β_s the normal and shear critical damping ratio respectively.

E^* [kPa]	μ [–]	β_n [–]	β_s [–]

1e6	0.0	0.2	0.0

Table 3. Hertz model microscopic parameters that rule PS-PF interactions with μ the friction coefficient, v the Poisson's ratio, G the shear modulus, β_n and β_s the normal and shear critical damping ratio respectively.

μ	v	G	β_n	β_s
[–]	[–]	[kPa]	[–]	[–]
0.0	0.3	3e6	0.2	0.0

Table 4. Summary of injection tests performed in a PS box.

Test	n_{sand} [–]	p_{sand} [kPa]	p_{inj} [kPa]
1	0.39	5	300
2	0.39	5	600
3	0.39	5	6000
4	0.42	5	300
5	0.42	5	600
6	0.42	5	6000
7	0.39	100	600
8	0.39	100	6000
9	0.42	100	600
10	0.42	100	6000

8. Figures

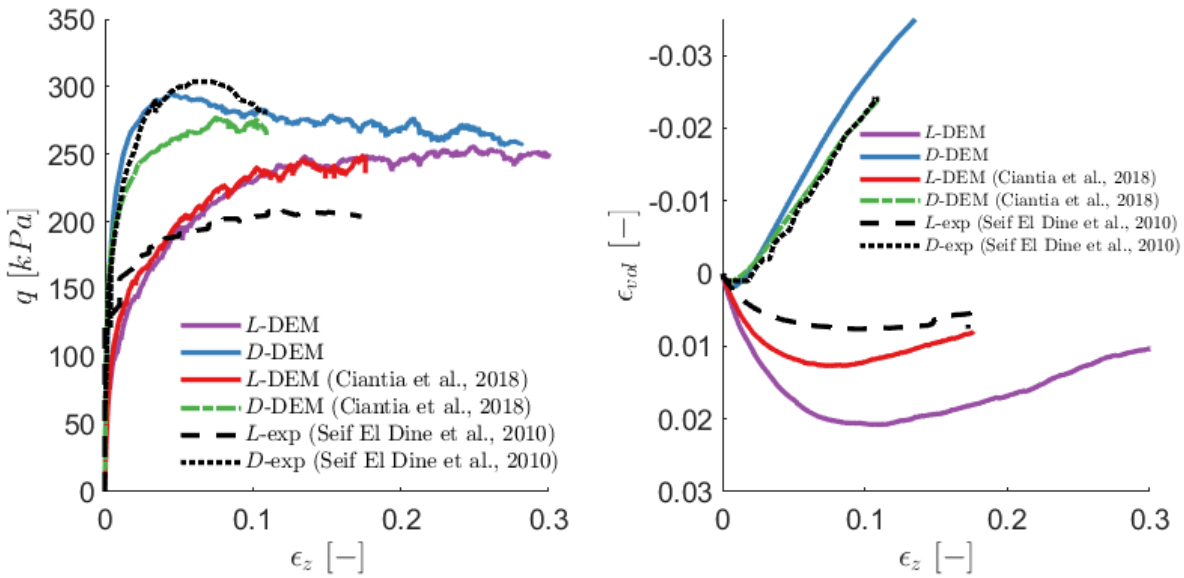

Figure 1. TX-CD tests; loose (L) and dense (D) PS specimens, p'$_c$ = 100 kPa.

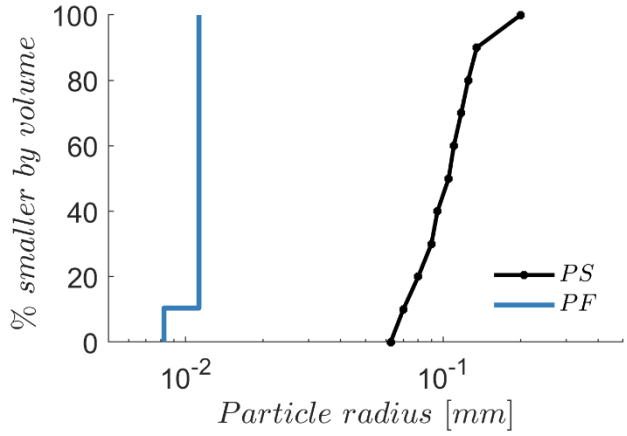

Figure 2. PSD comparison.

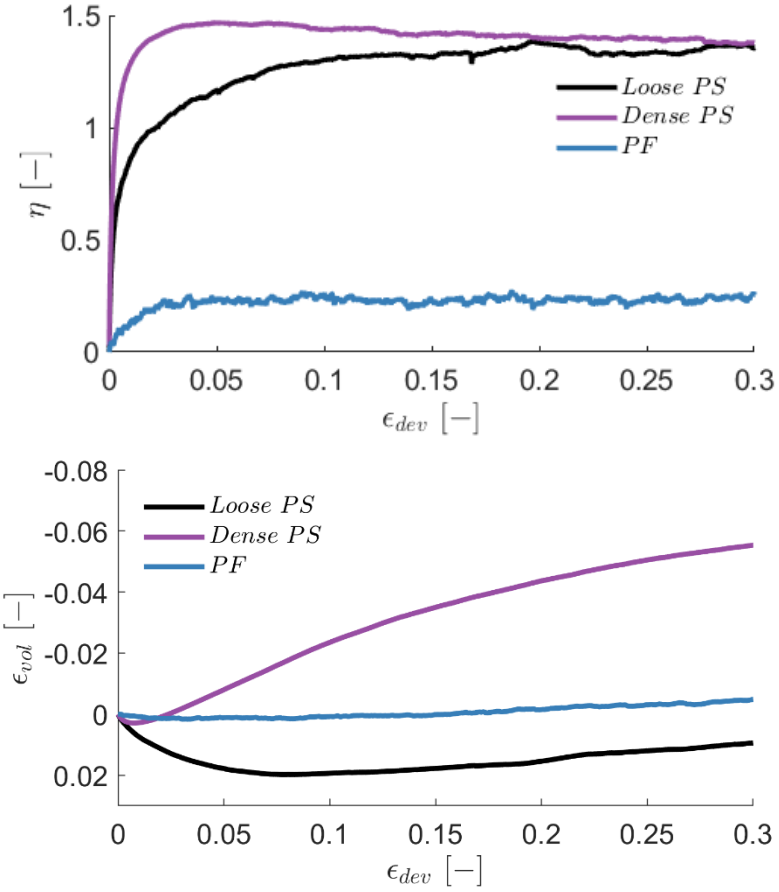

Figure 3. TX-CD tests comparison; p'_c = 200 kPa.

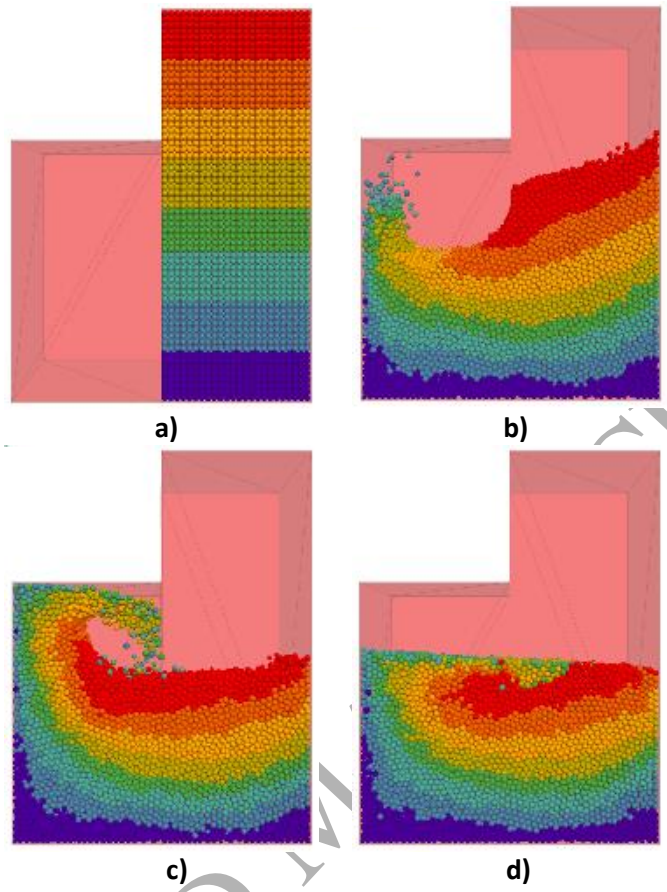

Figure 4. Time trend; PF BVP simulation, colour scale related to the initial z coordinate of PF particles (see **a)**).

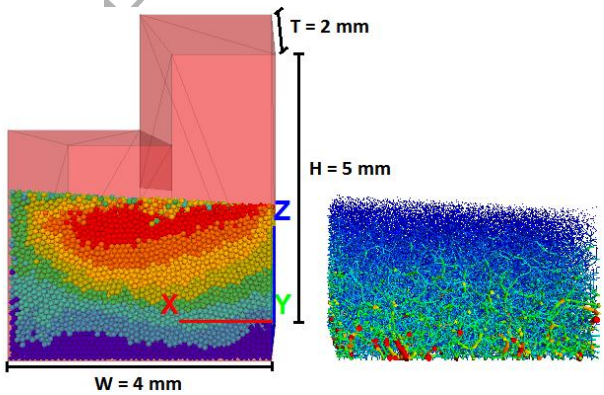

Figure 5. PF particles and contact forces; final time step, colour scale related to the initial z coordinate of PF particles (see Figure 4a).

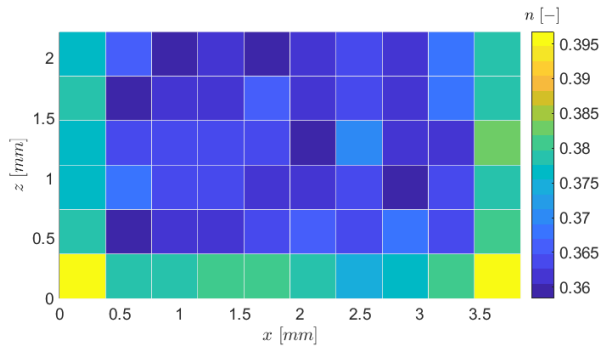

Figure 6. PF porosity contour; final time step, 0 mm < y < 2 mm.

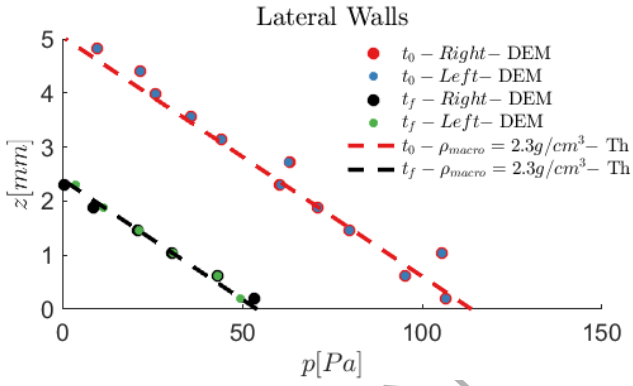

Figure 7. Pressure distributions acting on the lateral walls compared to the theoretical ones; initial (t_0) and final (t_f) time steps.

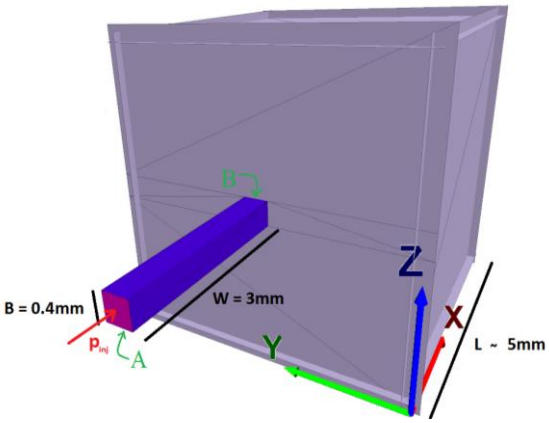

Figure 8. Geometry of mixture BVP.

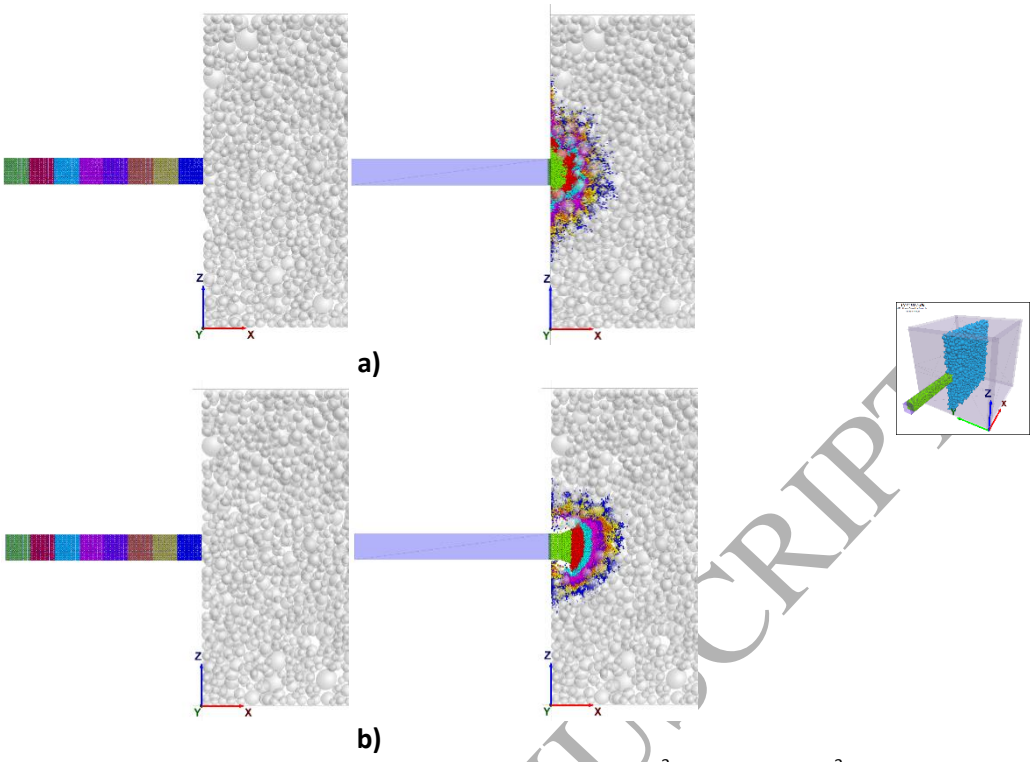

a)

b)

Figure 9. PF diffusion patterns; p_{sand} = 5 kPa, p_{inj} = 600 kPa, V_{inj} = 0 mm^3 and 0.48 mm^3; **a)** dense case, 2.2 mm < y < 2.6 mm; **b)** loose case, 2.4 mm < y < 2.8 mm.

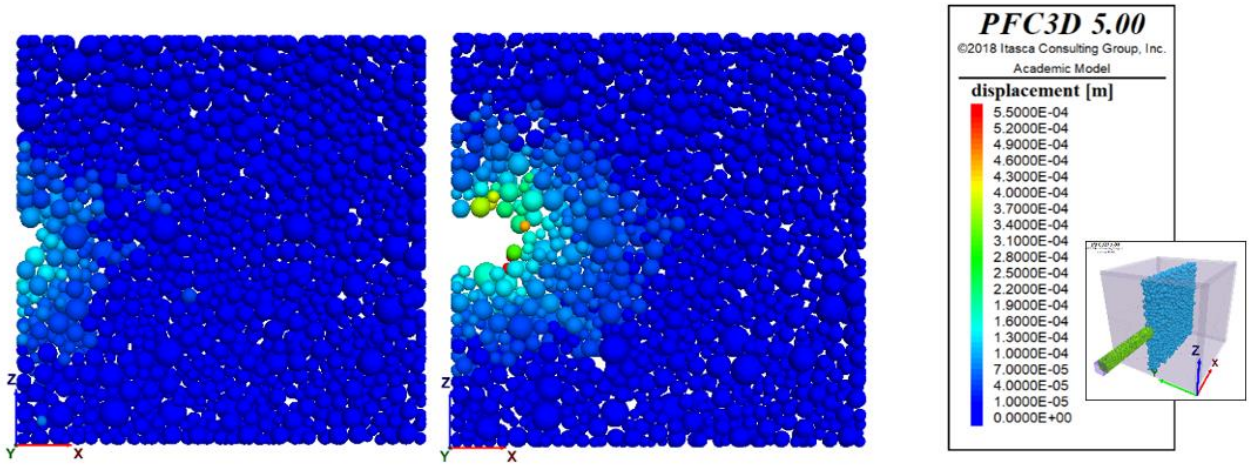

a) **b)**

Figure 10. PS induced displacements; p_{sand} = 5 kPa, p_{inj} = 600 kPa, V_{inj} = 0.48 mm^3; **a)** dense case, 2.2 mm < y < 2.6 mm; **b)** loose case, 2.4 mm < y < 2.8 mm.

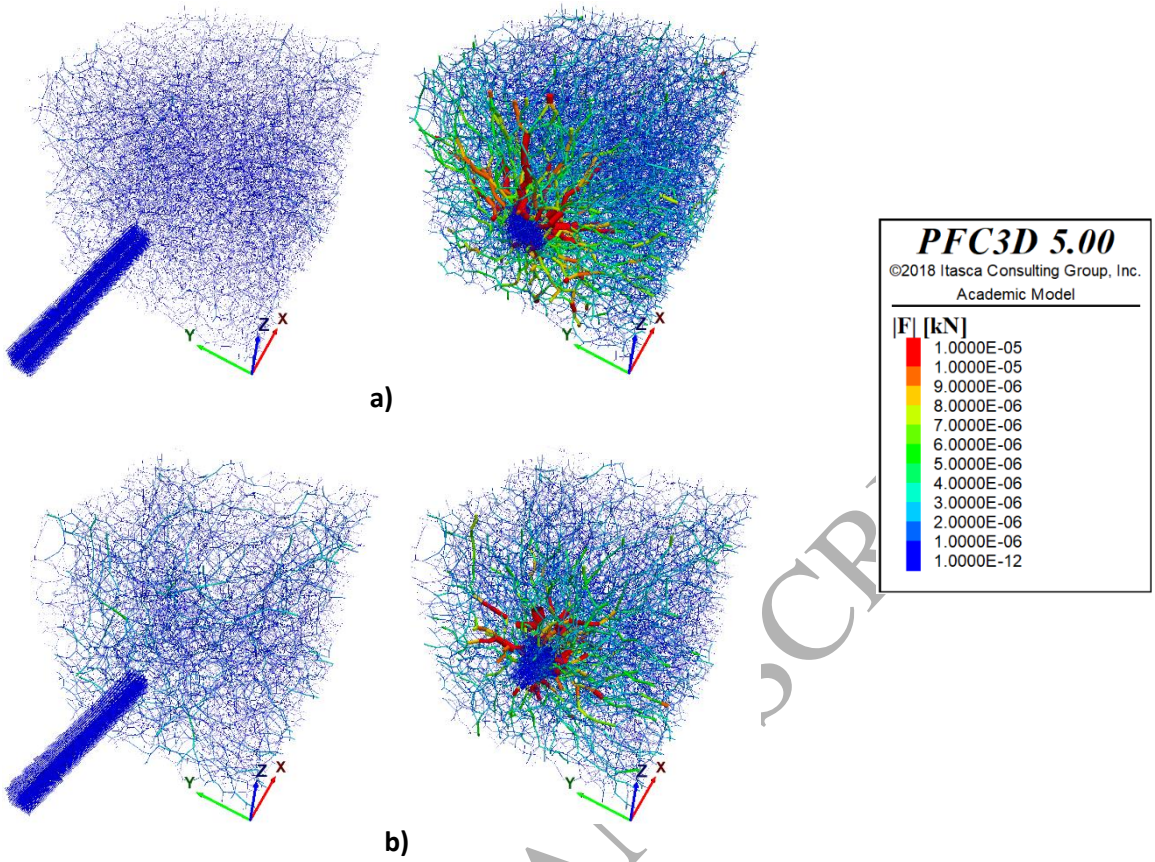

Figure 11. Contact forces; p_{sand} = 5 kPa, p_{inj} = 600 kPa, V_{inj} = 0 mm^3 and 0.48 mm^3; **a)** dense case; **b)** loose case.

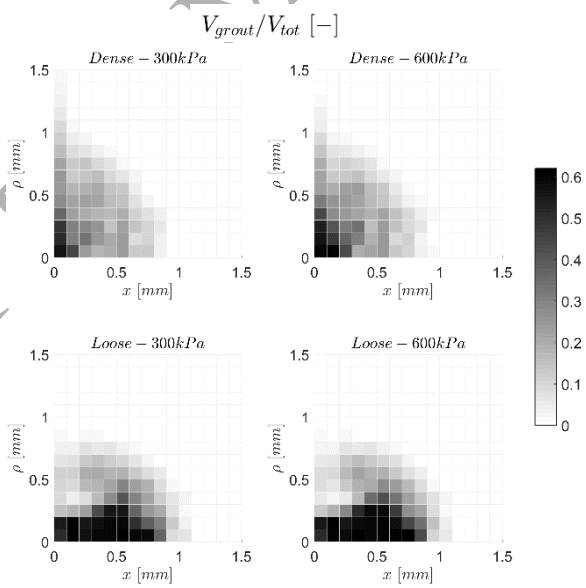

Figure 12. PF diffusion patterns and bulb shapes; volume of PF in each cylindrical crown (V_{grout}) with respect to corresponding total cylindrical crown volume (V_{tot}), hypothesis of axisymmetric conditions with respect to injection direction, V_{inj} = 0.48 mm^3, p_{sand} = 5 kPa.

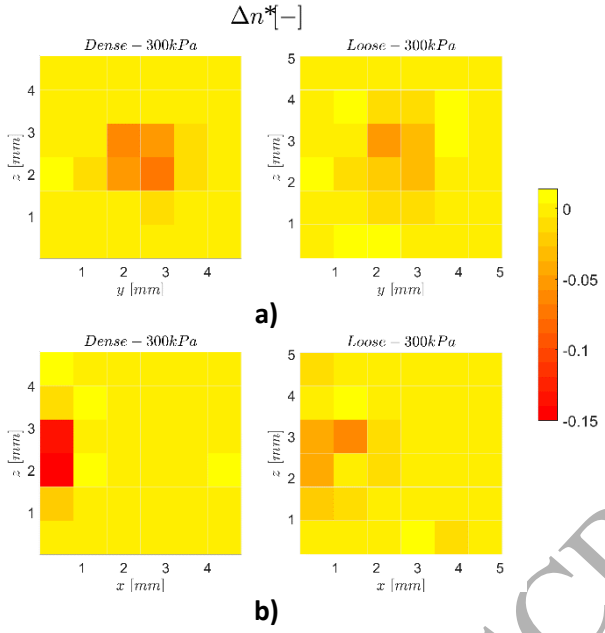

Figure 13. Local porosity variation (considering particles of both PS and PF); V_{inj} = 0.48 mm^3, p_{sand} = 5 kPa; **a)** y-z plane, 0 mm < x < 1.6 mm; **b)** x-z plane, 1.9 mm < y < 2.9 mm.

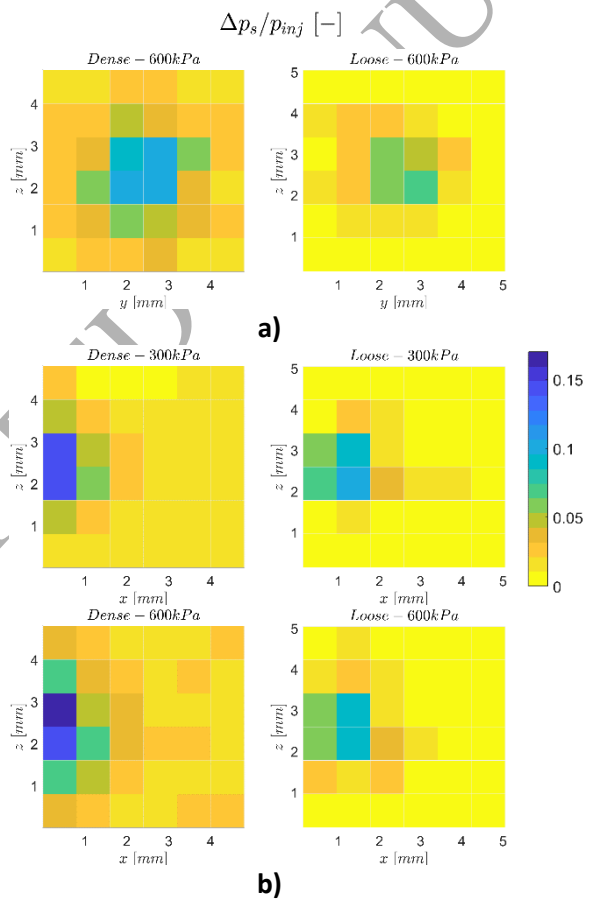

Figure 14. Increase in PS isotropic pressure (Δp_s) normalized with respect to injection pressure; V_{inj} = 0.48 mm^3, p_{sand} = 5 kPa; **a)** y-z plane, 0 mm < x < 1.6 mm; **b)** x-z plane, 1.9 mm < y < 2.9 mm.

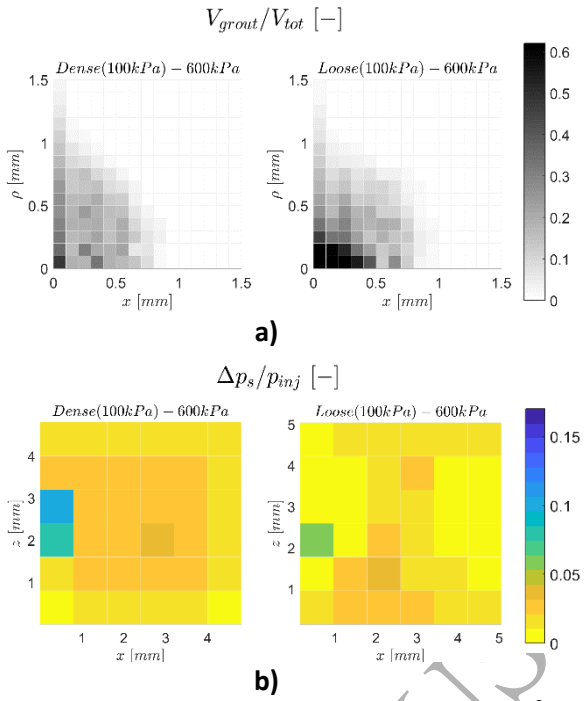

Figure 15. Initial PS isotropic pressure equal to 100 kPa; V_{inj} = 0.48 mm^3; **a)** volume of PF in each cylindrical crown with respect to corresponding total cylindrical crown volume, hypothesis of axisymmetric conditions with respect to injection direction; **b)** increase in PS isotropic pressure normalized with respect to injection pressure, x-z plane, 1.9 mm < y < 2.9 mm.

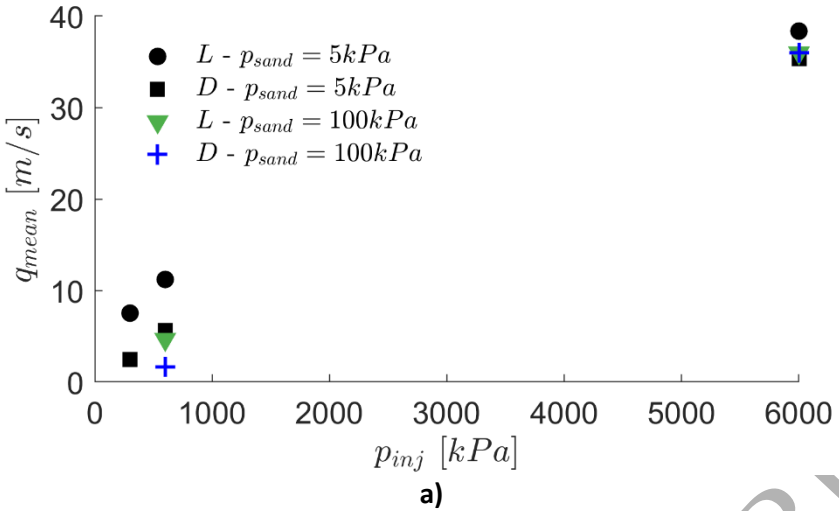

a)

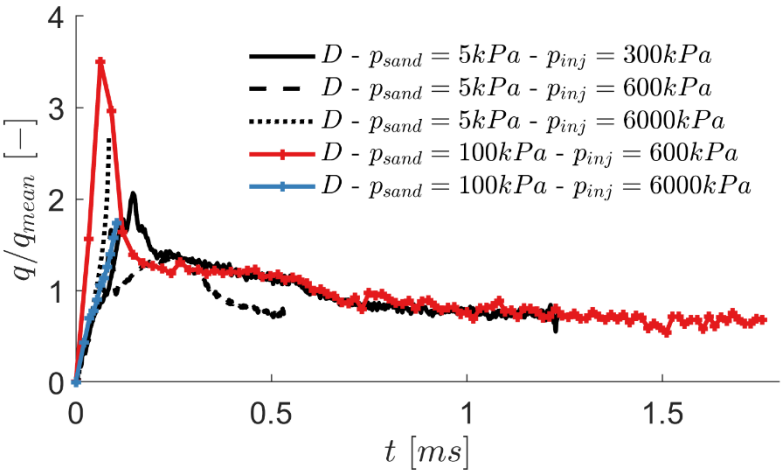

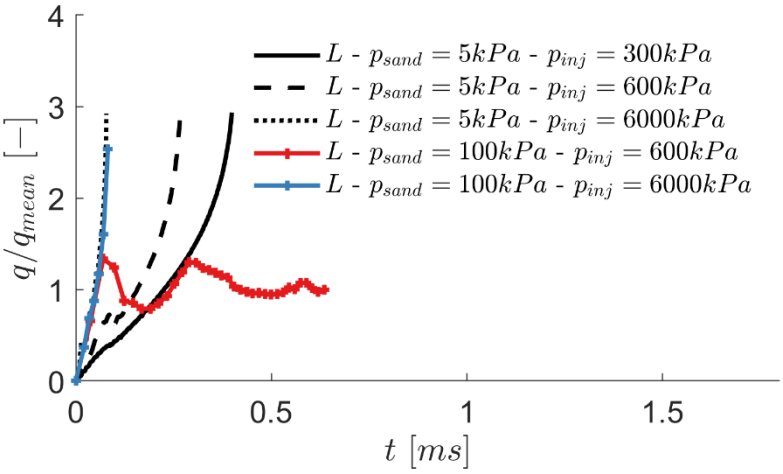

b)

Figure 16. Flow rates (Q) normalized with respect to fluid tube area (Q/A = q); V_{inj} = 0.48 mm^3; loose (L) and dense (D) PS; **a)** mean q; **b)** q evolution.

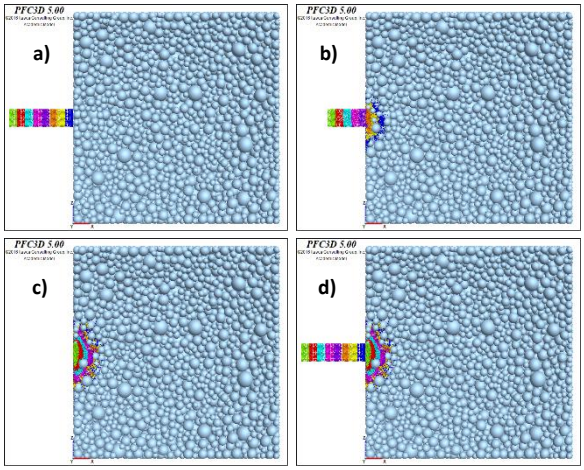

Figure 17. Brick repetition method; time trend.

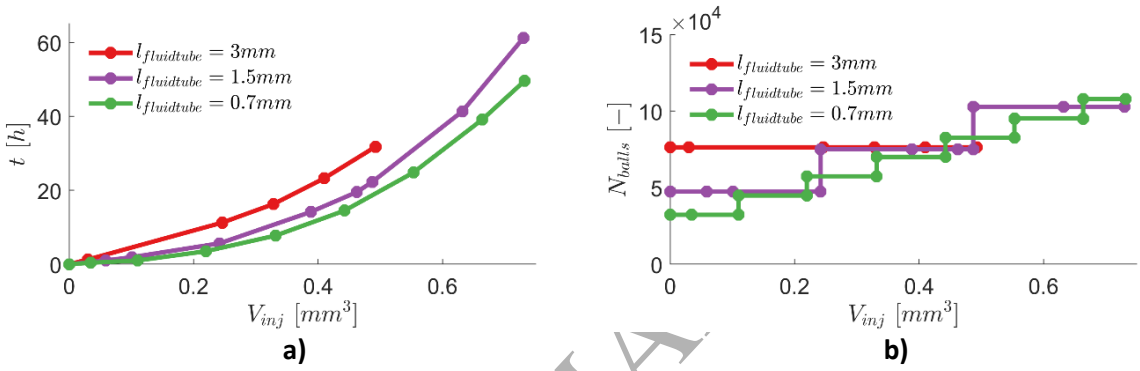

Figure 18. Computational times required to inject fixed volumes of PF employing various fluid tube lengths (**a)**) and correspondent number of particles step by step (**b)**); dense case, p_{sand} = 5 kPa, p_{inj} = 600 kPa.

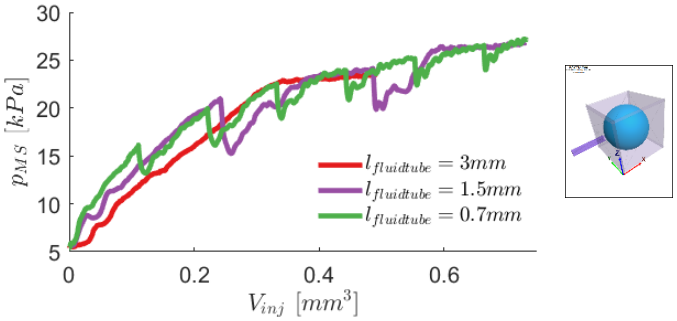

Figure 19. Evolution of isotropic pressure considering all particles inside the measurement sphere (MS) reported; dense case, p_{sand} = 5 kPa, p_{inj} = 600 kPa.

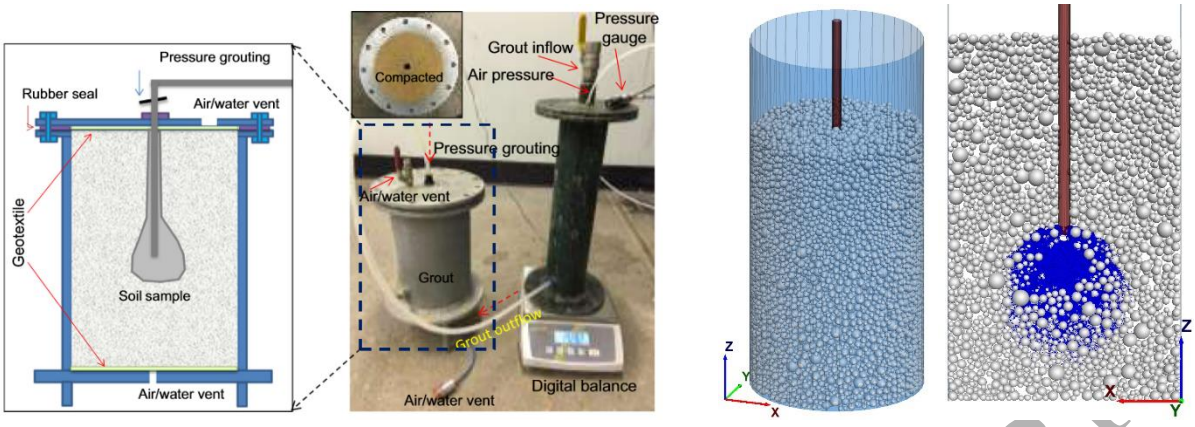

Figure 20. Laboratory-scale tests; **a)** lab test apparatus (Wang et al., 2016); **b)** correspondent DEM model.

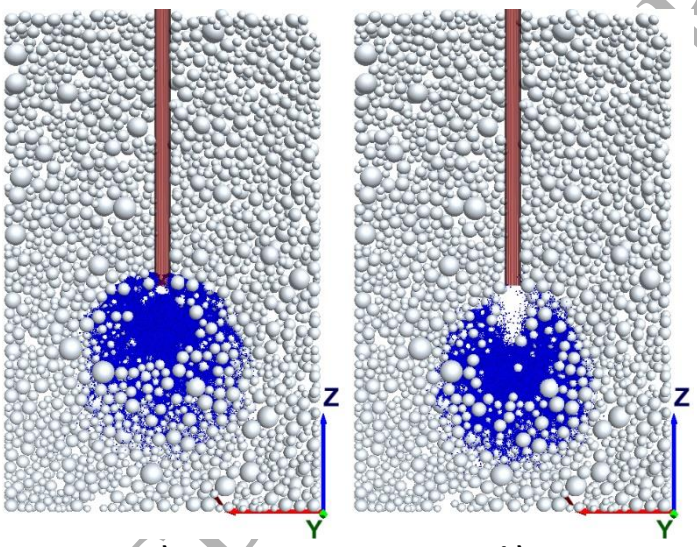

Figure 21. Particle spatial distributions; 95 mm < y < 105 mm, blue PF and grey PS; **a)** p_{inj} = 100 kPa, V_{inj} = 143 cm^3; **b)** p_{inj} = 300 kPa, V_{inj} = 159 cm^3.

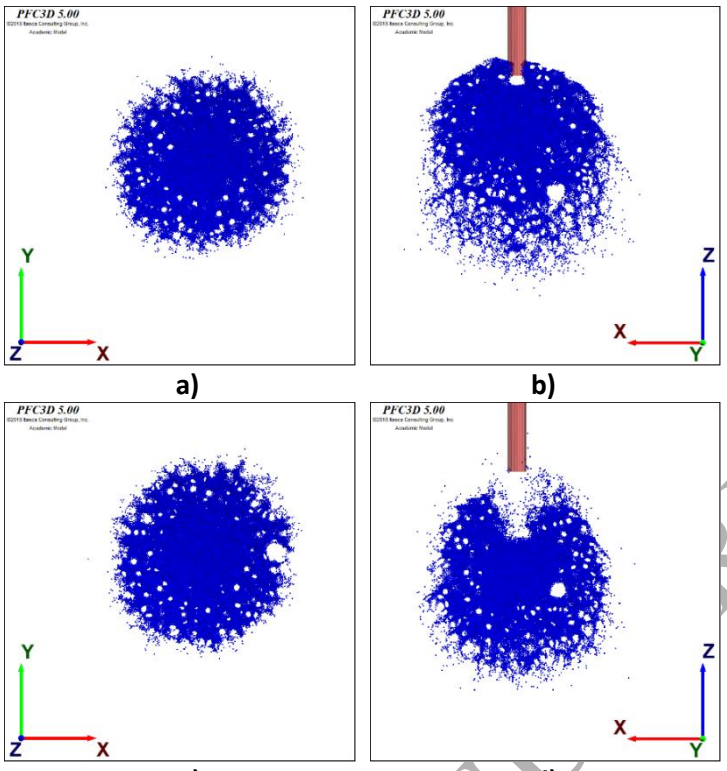

Figure 22. PF diffusion patterns; **a-b)** p_{inj} = 100 kPa, V_{inj} = 143 cm^3; **c-d)** p_{inj} = 300 kPa, V_{inj} = 143 cm^3; **a-c)** a 15 mm thick portion at a depth corresponding to maximum bulb radial dimensions; **b-d)** 92.5 mm < y < 107.5 mm.

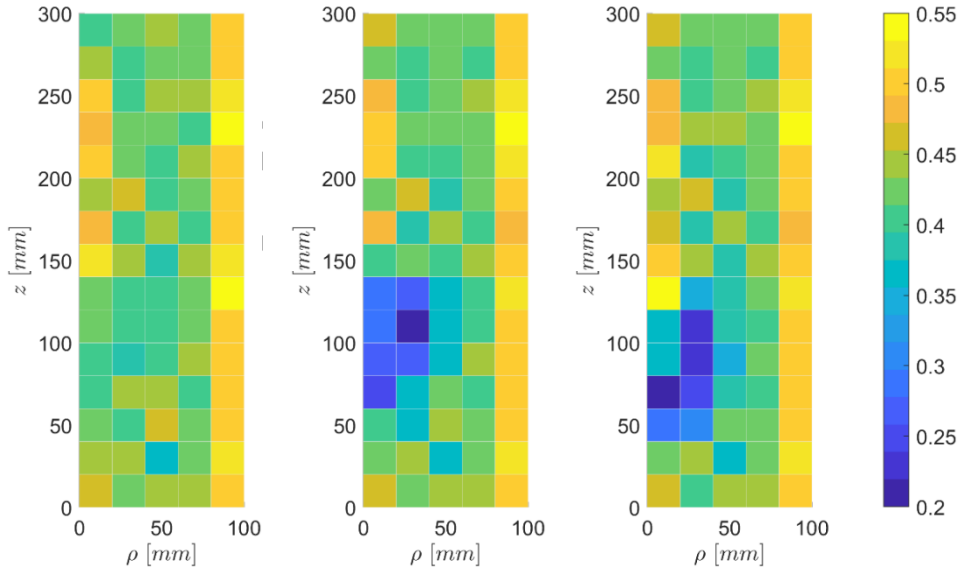

a) *n* [-] **b)** *n** [-] **c)** *n** [-]

Figure 23. Porosity contours (considering particles of both PS and PF); hypothesis of axisymmetric conditions with respect to injection direction; **a)** V_{inj} = 0 cm^3; **b)** p_{inj} = 100 kPa, V_{inj} = 143 cm^3; **c)** p_{inj} = 300 kPa, V_{inj} = 159 cm^3.

9. **Acknowledgements**

This research was funded by BASF SE within a research program aimed at numerically investigating and modelling the coupled hydro-mechanical processes governing grout injections.

10. **References**

ARROYO, M., BUTLANSKA, J., GENS, A., CALVETTI, F., JAMIOLKOWSKI, M., 2011. Cone penetration tests in a virtual calibration chamber. Géotechnique 61, 525–531.

BASF, n.d. BASF Launches Master Builders Solutions Professional Tradies Range. Constr. Eng. Aust. EPC Media Group, ISSN 2204-7247 Vol. 1, 14–15.

Bearce, R.G., Mooney, M.A., Kessouri, P., 2015. Estimation of Jet Grout Column Geometry using a DC Electrical Resistivity Push Probe 15–18.

Bezuijen, A., Van Tol, A.F., 2006. X-ray Tomography in Compensation Grouting Research: Shape and Density of Injected Grout. Adv. X-ray Tomogr. Geomaterials 355–363.

BOSCHI, K., 2018. Micromechanical investigation of grouting in soils. politesi.polimi.it.

Bui, H.H., Sako, K., 2007. Numerical simulation of soil–water interaction using smoothed particle hydrodynamics (SPH) method. J. Terramechanics 44, 339–346.

Calvetti, F., 2008. Discrete modelling of granular materials and geotechnical problems. Eur. J. Environ. Civ. Eng. 12, 951–965.

Catalano, E., Chareyre, B., Barthélemy, E., 2014. Pore-scale modeling of fluid-particles interaction and emerging poromechanical effects. Int. J. Numer. Anal. Methods Geomech. 38, 51–71.

Chareyre, B., Cortis, A., Catalano, E., Barthélemy, E., 2012. Pore-scale modeling of viscous flow and induced forces in dense sphere packings. Transp. porous media 94, 595–615.

Chen, X., Wang, J., 2014. A comparison of two-fluid model, dense discrete particle model and CFD-DEM method for modeling impinging gas–solid flows. Powder Technol. 254, 94–102.

Chialvo, S., Sun, J., Sundaresan, S., 2012. Bridging the rheology of granular flows in three regimes. Phys. Rev. E 85, 21305.

Ciantia, M., Arroyo, M., O'Sullivan, C., Gens, A., Liu, T., 2018. Grading evolution and critical state in a discrete numerical model of Fontainebleau sand. Géotechnique.

Ciantia, M.O., Arroyo, M., Butlanska, J., Gens, a., 2014. DEM modelling of a double porosity crushable granular material. Proc. Int. Symp. Geomech. from Micro to Macro 269–274.

Ciantia, M.O., Arroyo, M., Butlanska, J., Gens, A., 2016a. DEM modelling of cone penetration tests in a double-porosity crushable granular material. Comput. Geotech. 73, 109–127.

Ciantia, M.O., Arroyo, M., Calvetti, F., Gens, A., 2016b. A numerical investigation of the incremental behavior of crushable granular soils. Int. J. Numer. Anal. Methods Geomech. 40, 1773–1798.

Ciantia, M.O., Arroyo, M., Zhang, N., Emam, S., 2017. Periodic cells for large-scale problem

initialization. EPJ Web Conf. 140, 10–13.

Ciantia, M.O., Boschi, K., Shire, T., Emam, S., 2018. Numerical techniques for fast DEM large-scale model generation. Eng. Comput. Mech.

Covil, C.S., Skinner, A.E., 1994. Jet grouting—a review of some of the operating parameters that form the basis of the jet grouting process. In: Grouting in the Ground. pp. 605–629.

Cundall, P.A., 1987. Distinct element models of rock and soil structure. Anal. Comput. methods Eng. rock Mech. 129–163.

Dayakar, P., 2012. Study on Permeation Grouting Using Cement Grout In Sandy Soil. IOSR J. Mech. Civ. Eng. 4, 05-10.

Desrues, J., Viggiani, G., Besuelle, P., 2010. Advances in X-ray Tomography for Geomaterials. John Wiley & Sons.

Flora, A., Modoni, G., Lirer, S., Croce, P., 2013. The diameter of single, double and triple fluid jet grouting columns: prediction method and field trial results. Géotechnique 63, 934.

Frappin, P., Morey, J., 2001. Jet grouted column diameter measurement using the electric cylinder method. Soletanche Bachy. Intern. Publ.

Guo, Z., Shao, J., Shen, Y., Liu, M., 2013. Numerical simulation of soil-water jet interaction with smoothed particle hydrodynamics. In: 3rd International Conference on Particle-Based Methods. Fundamentals and Applications, Particles 2013; Stuttgart; Germany; 18 September 2013 through 20 September 2013. pp. 418–427.

Hatano, T., 2008. Scaling properties of granular rheology near the jamming transition. J. Phys. Soc. Japan 77, 123002.

Itasca, C.G.I., 2017. PFC — Particle Flow Code, Ver. 5.0.

Kenney, T.C., Chahal, R., Chiu, E., Ofoegbu, G.I., Omange, G.N., Ume, D.C.A., 1985. Controlling constriction sizes of granular filters. Can. Geotech. J 22, 32–43.

Krištof, P., Beneš, B., Křivánek, J., Šťava, O., 2009. Hydraulic erosion using smoothed particle hydrodynamics. In: Computer Graphics Forum. Wiley Online Library, pp. 219–228.

Leonardi, A., Wittel, F.K., Mendoza, M., Herrmann, H.J., 2014. Coupled DEM-LBM method for the free-surface simulation of heterogeneous suspensions. Comput. Part. Mech. 1, 3–13.

Madhyannapu, R.S., Puppala, A.J., Nazarian, S., Yuan, D., 2009. Quality assessment and quality control of deep soil mixing construction for stabilizing expansive subsoils. J. Geotech. geoenvironmental Eng. 136, 119–128.

Manenti, S., Sibilla, S., Gallati, M., Agate, G., Guandalini, R., 2011. SPH simulation of sediment flushing induced by a rapid water flow. J. Hydraul. Eng. 138, 272–284.

Meinhard, K and Adam, D and Lackner, R., 2010. Temperature measurements to determine the

diameter of jet-grouted columns. Proc. Int. Conf. Geotech. Challenges Urban Regen. 26--28.

Modoni, G., Croce, P., Mongiovì, L., 2006. Theoretical modelling of jet grouting. Géotechnique 56, 335–347.

Modoni, G., Wanik, L., Giovinco, G., Bzowka, J., Leopardi, A., 2015. Numerical analysis of submerged flows for jet grouting. Proc. - ICE Gr. Improv. 169, 1–12.

Morey, J., 1992. Les domaines d'application du Jet grouting 30, 17–30.

Munfakh, G.A., Abramson, L.W., Barksdale, R.D., Juran, I., 1987. In-situ ground reinforcement. In: Soil Improvement: A Ten Year Update. ASCE, pp. 1–66.

Nishimura, S., Takehana, K., Morikawa, Y., Takahashi, H., 2011. Experimental Study of Stress Changes Due To Compaction Grouting. Soils Found. 51, 1037–1049.

O'Sullivan, C., 2014. Particulate discrete element modelling: a geomechanics perspective. CRC Press.

Otsuki, M., Hayakawa, H., 2009. Critical behaviors of sheared frictionless granular materials near the jamming transition. Phys. Rev. E 80, 11308.

Paans, W.J.M., 2002. The influence zone and effectiveness of fracture grouting on piled foundations.

Peyneau, P.-E., Roux, J.-N., 2008. Frictionless bead packs have macroscopic friction, but no dilatancy. Phys. Rev. E 78, 11307.

Raivio, P., 2007. Technical Performance of Cementitious Grouting Materials for ONKALO Technical Performance of Cementitious Grouting Materials for ONKALO Laboratory Tests 2006.

Ribeiro, D., Cardoso, R., 2017. A review on models for the prediction of the diameter of jet grouting columns. Eur. J. Environ. Civ. Eng. 21, 641–669.

Rorato, R., Arroyo, M., Gens, A., Andò, E., Viggiani, C., 2017. THE EFFECT OF SHAPE IN GRANULAR MATERIALS: A GRAIN-SCALE STUDY OF THE KINEMATICS IN SHEAR BANDS. In: 3rd International Conference on Tomography of Materials and Structures.

Stefanova, B., Bubel, J., Grabe, J., 2012. Application of sph to erosion and excavation problems on the examples of jet grouting and offshore engineering. 7th Spheric 2012.

Stefanova, B., Seitz, K., Bubel, J., Grabe, J., 2012. Water–soil interaction simulation using smoothed particle hydrodynamics. In: Proceedings of the 6th International Conference on Scour and Erosion, Paris, France. pp. 695–704.

Ting, J.M., Corkum, B.T., Kauffman, C.R., Greco, C., 1989. Discrete Numerical Model for Soil Mechanics. J. Geotech. Eng. 115, 379–398.

Vescovi, D., Luding, S., 2016. Merging fluid and solid granular behavior. Soft Matter 12, 8616–8628.

Wang, Q., Wang, S., Sloan, S.W., Sheng, D., Pakzad, R., 2016. Experimental investigation of pressure grouting in sand. Soils Found. 56, 161–173.

Wang, Q., Ye, X., Wang, S., Sloan, S.W., Sheng, D., 2017. Use of photo-based 3D photogrammetry in

analysing the results of laboratory pressure grouting tests. Acta Geotech. 1–12.

Wang, S., Chan, D., Lam, K.C., 2009. Experimental study of the effect of fines content on dynamic compaction grouting in completely decomposed granite of Hong Kong. Constr. Build. Mater. 23, 1249–1264.

Wang, S.Y., Chan, D.H., Lam, K.C., Au, S.K.A., 2013. A new laboratory apparatus for studying dynamic compaction grouting into granular soils. Soils Found. 53, 462–468.

Wang, Z.-F., Shen, S.-L., Yang, J., 2012. Estimation of the Diameter of Jet-Grouted Column Based on Turbulent Kinematic Flow Theory. In: Grouting and Deep Mixing. pp. 2044–2051.

Yin, J., Chu, L., Su, L., 2005. Study on the interface shear strength of soil nails in a completely decomposed\rgranite soil by laboratory pullout tests and large-size direct shear box tests. Proc. 16th Int. Conf. Soil Mech. Geotech. Eng.